

Abyssal Pathways and the Double Silica Maximum in the Northeast Pacific Basin

Susan L. Hautala^{1,1} and Douglas E. Hammond^{2,2}

¹School of Oceanography

²University of Southern California

November 30, 2022

Abstract

This study examines causes of the double silica maximum in the deep interior Northeast Pacific Basin using a stochastic Lagrangian tracer model based on steady-state advective fields and diapycnal diffusion established by a hydrographic inverse method that conserves potential vorticity and salinity. Lateral diffusion, unresolved by the inverse model, is adjusted for overall agreement with radiocarbon distribution. The double silica maximum in vertical profiles arises from an eastern-intensified single-maximum in the North Pacific Deep Water along the northern domain boundary (originating in the western Pacific), and a strong subarctic bottom source supplying silica to Upper Circumpolar Deep Water density surfaces that successively intersect the seafloor over a broad area east of 150°W, associated geostrophically with southward flow. The existence of the double silica maximum requires weak diapycnal transport in the deep interior, with broader implications for the conceptual picture of meridional overturning circulation in the North Pacific.

Abyssal Pathways and the Double Silica Maximum in the Northeast Pacific Basin

Susan L. Hautala¹ and Douglas E. Hammond²

¹University of Washington.

²University of Southern California.

Corresponding author: Susan Hautala (hautala@uw.edu)

Key Points:

- An upper (North Pacific Deep Water) silica maximum is advecting through this region with only minor modification
- A lower (Upper Circumpolar Deep Water) maximum is created locally by density structure, flow pathways and enhanced subarctic seafloor flux
- The existence of the double silica maximum is linked to weak diapycnal mixing, with broader implications for North Pacific overturning

Abstract

This study examines causes of the double silica maximum in the deep interior Northeast Pacific Basin using a stochastic Lagrangian tracer model based on steady-state advective fields and diapycnal diffusion established by a hydrographic inverse method that conserves potential vorticity and salinity. Lateral diffusion, unresolved by the inverse model, is adjusted for overall agreement with radiocarbon distribution. The double silica maximum in vertical profiles arises from an eastern-intensified single-maximum in the North Pacific Deep Water along the northern domain boundary (originating in the western Pacific), and a strong subarctic bottom source supplying silica to Upper Circumpolar Deep Water density surfaces that successively intersect the seafloor over a broad area east of 150°W, associated geostrophically with southward flow. The existence of the double silica maximum requires weak diapycnal transport in the deep interior, with broader implications for the conceptual picture of meridional overturning circulation in the North Pacific.

Plain Language Summary

Silica, an important nutrient supporting diatom production, has two distinct vertical concentration maxima in the deep (>1000 m) northeast Pacific ocean. This structure suggests that distinct processes create each of these features. In this study, we explore how large-scale deep ocean circulation, quantified by a recent study, combines with a simple latitude-dependent source of silica from seafloor sediments to create a near-bottom maximum within a southward current in the densest layers in the eastern half of the basin. In contrast, a shallower (mid-depth) silica maximum in the vertical structure of concentration profiles is already present in the inflowing deep water, and is not substantially modified as it flows through this part of the ocean.

1 Introduction

Deep water mass modification in the Northeast Pacific Basin (NEPB) is poorly understood. Indicators of water "age", such as radiocarbon, are intensified at mid-depth, and the region has been described as a *cul-de-sac* of the planetary overturning circulation, where abyssal water is converted into mid-depth water by unresolved processes (e.g. Schmitz 1995). The existence of a double maximum in silica concentration (Si) – one near 2500 m, and another at the bottom near 4000 m (Edmond et al., 1979) – contraindicates direct upwelling of bottom water and raises questions about how these two maxima are maintained (Talley and Joyce 1992). In this study, three-dimensional, steady-state advection fields from a hydrographic inverse model (Hautala 2018, hereafter H18) are used in a stochastic Lagrangian forward simulation (e.g., van Sebille et al. 2018) of silica, carbon and radiocarbon concentration, with the latter included because it constrains residence time. Lessons learned from this regional analysis have implications for how the broader Pacific overturning circulation is structured in the presence of weak interior diapycnal mixing.

2 Methods

The model domain lies north of 20°N and east of 170°E. Because the Mendocino Fracture Zone (Figure 1a) presents a barrier to exchange, distinct pools of dense Lower Circumpolar Deep Water (LCDW) fill isolated deep areas to its north and south (Tsunogai 1987; Fig. 3 of H18). In order to model trajectories spanning the entire basin, the analysis is confined to

the North Pacific Deep Water (NPDW: $28.01 > \gamma > 27.70$) and Upper Circumpolar Deep Water (UCDW: $28.10 > \gamma > 28.01$) following the definitions of MacDonald et al. (2009).

Ensemble averages are constructed from 100 realizations, each with 162 Lagrangian trajectories seeded at nominal 1° spacing on each of 24 neutral surfaces within this density range (for exact values, see H18). Initial tracer concentrations were specified near the domain edges by interpolating selected water sample profiles using Ocean Data View and the GLODAPv2 data base (Olsen et al. 2016; Key et al. 2015) (Figure 1c, S-A1). A northern initialization line roughly parallels the Aleutian Trench. Western and southern lines are defined at 180° (P14 section) and at 21°N (linearly interpolating P3 and P4). A short southeastern line from 20°N to 30°N along 121°W also interpolates the P3 and P4 sections.

Because the inverse model is designed to resolve $\sim\text{mm/s}$ large-scale interior abyssal circulation (using a planetary geostrophic potential vorticity conservation equation), it does not resolve narrow $\sim\text{cm/s}$ boundary currents, particularly the Aleutian deep boundary current (DBC) system (Warren and Owens 1985). We assume that strictly southward flow supplies tracer, at a specified concentration, from the Aleutian DBC to seed locations at the irregular northern edges of each neutral surface, estimated at 1° resolution. This assumption is consistent with the overall pattern of abyssal circulation (Figure 1a, see also H18), although there may be some modification of tracer concentration along these short sections, or unresolved pathways from nearby longitudes. If the neutral surface edge lies south of 47°N , or if the normal component of velocity at an initialization location is directed out of the domain, then the seed is not initialized.

Using a 6-month time step, Δt , water parcel locations are iterated in two stages. In the first (advective) stage, a displacement vector, $\underline{\Delta x} = (u\Delta t, v\Delta t, \Delta\eta + e\Delta t)$, is calculated using eastward (u) and northward (v) geostrophic velocity, and diapycnal velocity (e), from the inverse model. Water parcels largely follow neutral surfaces, and the isoneutral component of vertical displacement, $\Delta\eta$, is the difference in neutral surface height at the new position and the previous time step. Values between inverse model grid points are determined by linear interpolation. In the second (diffusive) stage, water parcels are randomly displaced by a value drawn from a Gaussian distribution with a specified standard deviation as follows.

Diapycnal stochastic displacements are based on diapycnal diffusivity, K_V , from the inverse model. Each geographical location yields a unique coefficient multiplying a vertical structure function motivated by observations (Kunze et al. 2006) and depending on stratification, bottom roughness and height above the bottom (see H18 for details). The diapycnal displacement standard deviation, $\sigma = \sqrt{2K_V\Delta t}$ (e.g., Taylor 1921), is thus a three-dimensional field with weak interior values and isolated mixing hotspots linked to bottom roughness (i.e., Kunze et al. 2006). The inverse solution's maximum isoneutral average K_V is only $2.4 \times 10^{-6} \text{ m}^2 \text{ s}^{-1}$ ($\sigma = 6 \text{ m}$ after 6 months) found on a neutral surface with a mean depth of $\sim 4200 \text{ m}$.

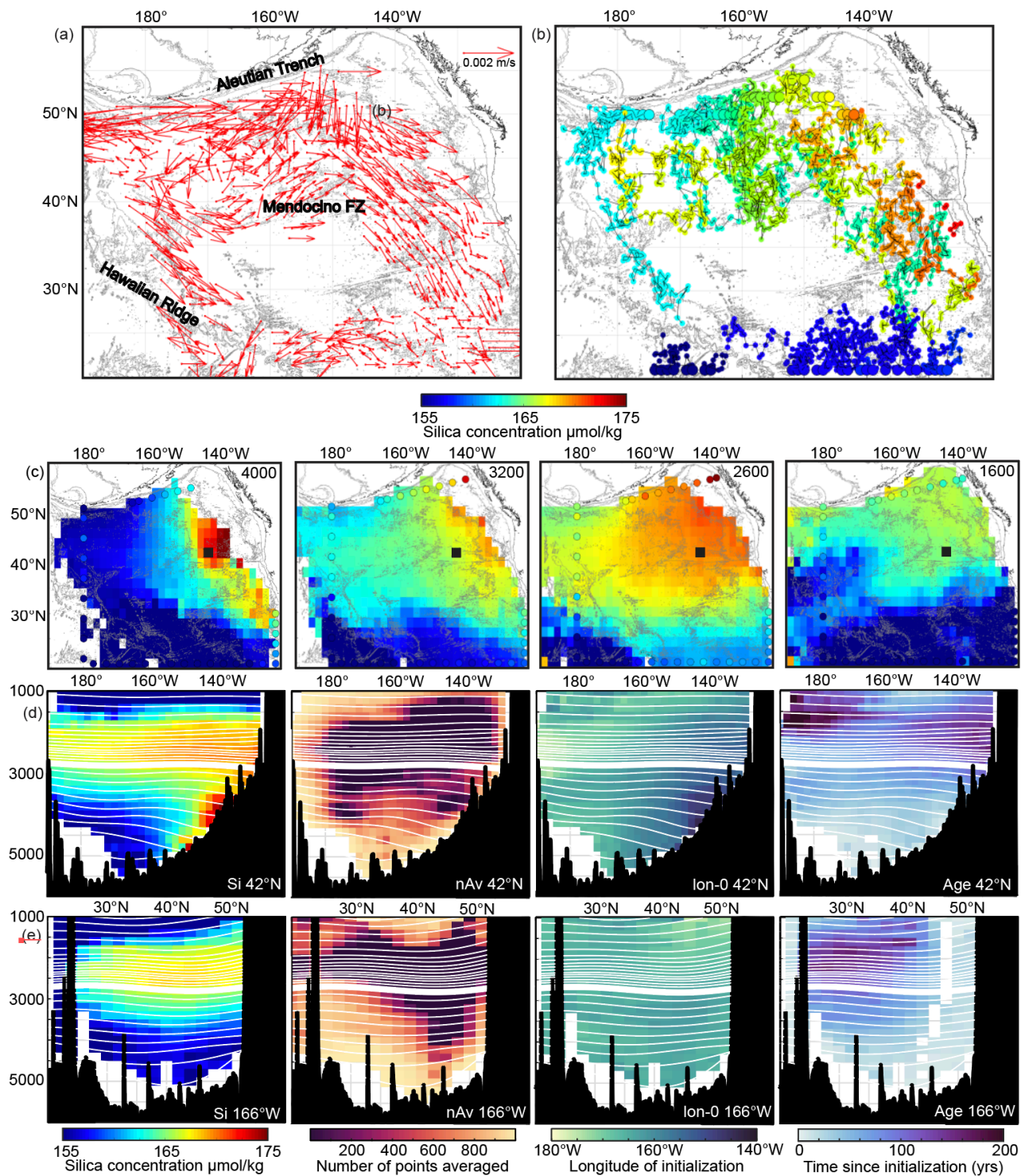


Figure 1. (a) Geostrophic current vectors for one realization of Lagrangian trajectories on $\gamma = 28.047$ (average pressure 3147 dbar) in the UCDW, with 0.5' SRTM30-PLUS bathymetry (Becker et al., 2009; Sandwell and Smith, 2009). For clarity, locations within 1° are not shown. (b) As in (a) but for Si, with initial values larger and edged in black. The color bar for all silica plots appears below the top row. (c) Bin-average Si on constant pressure planes as indicated (dbar). The black square marks (42°N , 142°W), and white areas are outside the model domain. Colored circles indicate initial concentration. Vertical sections along (d) 42°N and (e) 166°W , from left to right: Bin-average Si, number of points averaged, average longitude of trajectory initialization, and average years of trajectory integration to that point. White lines indicate neutral surfaces, with the uppermost UCDW model surface, $\gamma = 28.016$, thickened.

In H18, lateral diffusivity, K_H , was parameterized as a function of neutral density, but values were not statistically significant within error bars reaching $200 \text{ m}^2/\text{s}$ at mid-depth. The use of this inverse solution K_H produces a basin-averaged low bias in both radiocarbon and silica, compared to observational values determined by linearly interpolating the model fields to bottle locations from four sections (Figure 2, S-C1) that cross the NEPB (*P17*: Musgrave et al. 1995; *P16-2006*: Feely et al. 2013; *P01-2007*: Kawano et al. 2009; *P02-2012*: Swift et al. 2014). Increasing K_H reduces residence time and improves the agreement with radiocarbon.

Guided by the inverse model, we took $200 \text{ m}^2/\text{s}$ as an approximate upper bound on K_H , corresponding to a lateral displacement standard deviation $\sigma = 79 \text{ km}$. We iteratively increased σ from 40 to 100 km ($K_H = 51$ to $322 \text{ m}^2/\text{s}$), re-running the inverse calculation each time to solve for slightly modified velocity fields (Supplement, Section D). We settled on $\sigma = 90 \text{ km}$, corresponding to $K_H = 260 \text{ m}^2/\text{s}$. This value is less than half that of the “LOW-ISO” run from DeVries and Holzer (2019). However, tracer release experiments in the abyssal Brazil Basin are consistent with even lower values (Rye et al. 2012). Lower values of K_H improve the fit to potential vorticity and salinity conservation equations in the inverse model. Additionally, because of increased time exposed to sources, lower values of K_H produce Si fields in better agreement with the data (Figure S-D1), particularly more realistic (higher) concentrations in the near-bottom maximum (Figure S-D5). However, given the clear radiocarbon bias at these low values, we selected a run with higher K_H for interpretation. The sensitivity of specific results to K_H is discussed below.

Next, we determine conditions for ending integration of trajectories, beginning with water parcels leaving the domain across 170°E or 20°N . Water parcels encountering interior topographic obstacles (i.e., missing value holes in the inverse domain) are assumed to enter a narrow, unresolved boundary current, and flow around the obstacle rather than dead-ending. In these cases, a “boundary current slippage” algorithm is implemented. First, we divide the basin into two regions. The western region is between 173°W and 150°W , and north of the Hawaiian Ridge, defined as a line from (20°N , 150°W) to (32°N , 170°E). Here, upon encountering a topographic hole, the velocity is set purely eastward (i.e., back toward the interior) for one time step at the same speed prior to encounter. The eastern region is between 150°W and 123°W and north of 20°N . Here, the velocity is set to purely westward (again, back toward the interior). Tracer concentration is not changed during boundary current slippage, and integration is halted after 20 sequential slippage time-steps (some water parcels become “stuck” by repeatedly re-entering topographically masked regions). In the eastern region, this process can be activated

where neutral surfaces intersect the broad topographic slope. However, the density structure in these areas is such that geostrophic flow is predominantly along rather than across topographic contours. Thus, when the smaller across-topography component of flow results in trajectories leaving the domain, intermittent redirection into the nearest interior box has only a minor impact on the trajectories. Very few water parcels remain stuck in the interior after the maximum integration time of 500 years (Figure 3a, solid vs. dashed lines). The double silica maximum occurs without boundary slippage (Fig. S-D4), but with fewer points to average overall, particularly in the UCDW.

Finally, we use existing observations to specify tracer source/sink functions that determine concentration changes after each time-step. Silica and carbon fields are both affected by water column regeneration from sinking biogenic particulates, with rates established by sediment trap observations. The rain of particulates into the deep ocean varies considerably between the subtropical and subarctic gyres, with a transition zone between them. We define three corresponding areas by latitude: Zone 1: 20-35°N, Zone 2: 35-40°N and Zone 3: > 40°N.

For silica, the latitude dependence is particularly strong, as shown by benthic flux estimates from pore water profiles and core incubations, as well as a compilation of deep trap deployments (Hou et al., 2019). This compilation is used to estimate the Si rain at 1 km depth for each zone. Hammond et al. (2004) estimated about 5% of the Si rain dissolves as it sinks from 1 to 4 km, a fraction too small to detect in most sediment trap deployments (Wong et al., 1999). The 5% value is adopted here for zones 1 and 2, with a value of 15% for Zone 3, based on trap data at station P (50°N, 145°W, Wong et al. 2008). Only a few percent of the silica rain is permanently buried (Hou et al. 2019), so the rain reaching the seafloor is assumed to diffuse back into the deepest layer from the upper sediments, creating a bottom source. A sensitivity experiment explored a different value for the fraction dissolving in the water column. The double maximum is not sensitive to the larger fraction specified for Zone 3, nor to changes in source parameters by factors of two (Supplement, Section D).

Based on these observations, we specify both a water column regeneration source, $Si_R = (1, 10, 90) \text{ mmol m}^{-2} \text{ y}^{-2}$ for Zones 1, 2, and 3, respectively and a bottom source, $Si_B = (20, 200, 600) \text{ mmol m}^{-2} \text{ y}^{-2}$. The water column source is distributed over the entire water column thickness (H), whereas the bottom source affects only water parcels in the deepest neutral surface layer, with a strength that depends on the height of the water parcel above the bottom (h). Thus, the rate of change of Si is, in $\mu\text{mol kg}^{-1} \text{ y}^{-1}$,

$$\frac{\Delta Si}{\Delta t} = \frac{1000}{\rho_0} \left(\frac{Si_R}{H} + \frac{Si_B}{h} \right)$$

where the nominal ocean depth $H = 5000 \text{ m}$, $\rho_0 = 1025 \text{ kg/m}^3$, and the factor of 1000 has units of $\mu\text{mol}/\text{mmol}$.

Unlike silica, the carbon rain, C_R , is a strong function of pressure. An estimate of the organic carbon rain rate for Zone 3 and its depth dependence is specified using a power law Martin function (Martin et al., 1987) with the exponent, $b=0.575$, determined via a fit to sediment traps deployed from 200 to 4200 m depth at station P (50°N, 145°W; Wong et al. 2008). This value is close to that recommended by Marsay et al. (2015). Similarly, $b=0.235$ for CaCO_3 . The decrease in particulate flux as material settles through each layer should equal the remineralization rate, so the derivative of the Martin function for each phase has been used to

determine the carbon input from both organic C and CaCO₃ particulates. Carbon burial is assumed to be negligible.

The resulting rate of carbon input is, in $\mu\text{mol kg}^{-1} \text{y}^{-1}$:

$$\frac{\Delta C}{\Delta t} = \frac{1000}{\rho_0} (C_R + C_B).$$

with the following structure functions (derived from the Martin function) summing inorganic and inorganic input, specifying dependence on scaled pressure, $\hat{p} = p/200$ dbar (in $\text{mmol m}^{-3} \text{y}^{-1}$),

$$C_R = F_R (1.590 \hat{p}^{-1.575} + 0.354 \hat{p}^{-1.235})$$

$$C_B = 1000 \frac{F_R}{h} (0.553 \hat{p}^{-0.575} + 0.301 \hat{p}^{-0.235}).$$

Carbon fluxes for Zones 1 and 2 are taken as a fixed percentage of the Zone 3 value such that $F_R = (0.25, 0.50, 1.00)$ for Zones 1, 2 and 3, respectively. Example values ($\text{mmol m}^{-3} \text{y}^{-1}$) for Zone 3 at 1000 dbar are $C_R = 0.175$; at 4000 dbar: $C_R = 0.023$, and $C_B \times h/1000 = 0.248 \text{ mol m}^{-2} \text{yr}^{-1}$.

Pre-bomb surface water $^{14}\text{C}/^{12}\text{C}$ ratios, $F_{C14} = (0.95, 0.93, 0.90)$ for Zones 1, 2 and 3, respectively, have been used to specify the ^{14}C of remineralized carbon; bomb contamination makes only a minor contribution to ^{14}C below 1 km, given the 1-2 kyr residence time of the water at depth. Our specified function for the rate of change of radiocarbon concentration includes this fractionation along with a decay constant, $\lambda = 1.209 \times 10^{-4} \text{y}^{-1}$, such that:

$$\frac{\Delta^{14}\text{C}}{\Delta t} = F_{C14} \frac{\Delta C}{\Delta t} - \lambda^{14}\text{C}.$$

3 Results

We examine Eulerian fields to understand the causes of the double silica maximum. These are created from the Lagrangian trajectory data by ensemble-averaging values from all 100 realizations in $2^\circ \times 2^\circ \times 200$ dbar bins (Figure 1). Trajectories do not sample the deepest parts of the basin (white areas of Figure 1d,e), where there are isolated pools of LCDW. Outside these unresolved areas, the model predicts the overall tracer structure relatively well, particularly the existence of the double silica maximum in the eastern NEPB (Figure 2). The average absolute difference from observations between 1500-3500 dbar is about 1% for silica and radiocarbon and less for total carbon (Figure S-D1). Between 1500 and 3500 dbar, the standard deviation of tracer difference from observations is: radiocarbon – 6.9‰, silica – 6.1 $\mu\text{mol/kg}$ and total carbon – 11.5 $\mu\text{mol/kg}$. This degree of misfit for radiocarbon is similar to that of DeVries and Holzer (2019). Si in the near-bottom maximum is underpredicted by the preferred model run (Fig. 2). The underlying model still has oversimplified aspects, particularly the specification of constant lateral diffusivity and an estimated uncertainty of ~30% in the Zone 3 tracer source. Nevertheless, a double silica maximum forms for all input parameter variations that were explored, unless the bottom source is set to zero (Supplement, Figure S-D5).

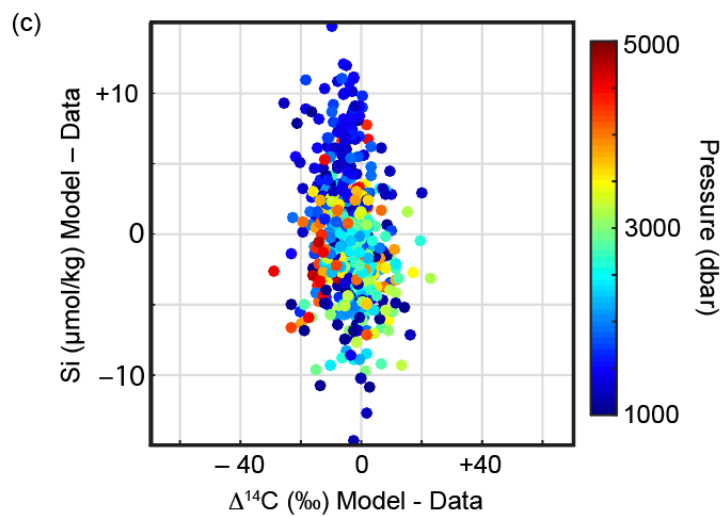
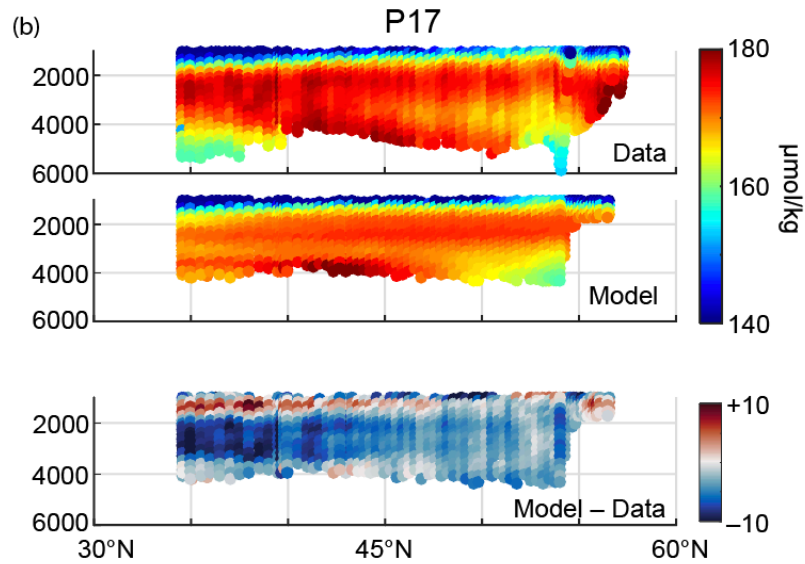
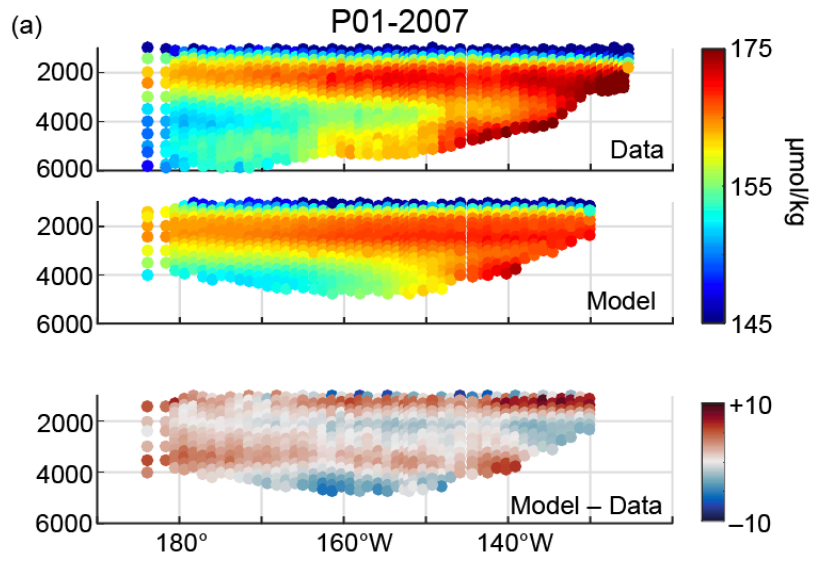


Figure 2. Vertical sections of modeled and observed Si along (a) P01-2007, $\sim 47^\circ\text{N}$ and (b) P17. The model does not extend as deeply as the data; the domain excludes disconnected deep pools of LCDW in the northern and southern NEPB. (c) Differences (model minus observed) for ^{14}C vs Si using data from all four comparison sections.

Figure 3a shows basin-averaged silica concentration as a function of time since initialization, averaged over all trajectories. Also shown is the histogram of time spent within the basin. The inferred bulk transit time is roughly 40-100 years, larger in the NPDW than the UCDW. Concentration changes more rapidly near the beginning of integration, reflecting input beneath the subarctic gyre with its higher silica flux, particularly for the UCDW. However, there is considerable geographic variation in silica addition (Figures 3c, S-B2), due to the strong bottom source where neutral surfaces ground into topography. Here, rates of silica addition reach $2 \mu\text{mol kg}^{-1} \text{yr}^{-1}$ at 4000 dbar (Figure S-B3) associated with the southward near-bottom current in the eastern half of the basin.

4 Discussion and conclusions

A double silica maximum is not found in the boundary conditions (Figures 1c, S-A1). A vertical structure with a mid-depth (NPDW) maximum is set up outside the model domain by lower silica water of southern origin underlying “older” mid-depth water in the low-latitude western Pacific, augmented by high Si water that flows out of the Bering Sea along the western boundary of the Kamchatka Strait (i.e., Reed et al. 1993), where Si exceeds $200 \mu\text{mol/kg}$ between 2 and 3 km depth. The signal is diluted by mixing between deep counterflows in the Kuril-Kamchatka and Aleutian Trenches (Owens and Warren 2001), but, due to weak diapycnal mixing, a single maximum in the lower NPDW persists as water moves east in the Aleutian DBC to form the westernmost profile of the northern initialization line (51°N , 180°). Along the northern initialization line, values of the NPDW maximum ($\gamma = 28.0$) increase eastward from $166 \mu\text{mol/kg}$ to $177.3 \mu\text{mol/g}$ at (56.7°N , 137°W). Even a uniform addition along the Aleutian Trench, creating this zonal gradient in initial concentration, would make it appear as if the mid-depth maximum originates in the northeast Pacific, whereas its vertical structure is already present in the northwest. Values at $\gamma = 28.1$ (the bottom of the UCDW) also increase towards the east, by an even greater amount than at mid-depth (153.2 to $176.1 \mu\text{mol/kg}$). However, the near-bottom maximum develops only after UCDW water parcels begin to flow south and are exposed to high benthic flux within the interior of the NEPB, particularly north of 40°N .

Previously, Talley and Joyce (1992) calculated that an addition of about $0.2 \mu\text{mol L}^{-1} \text{yr}^{-1}$ is needed to maintain the mid-depth silica maximum. Their budget assumed the average North Pacific silica increases by $20 \mu\text{mol/L}$ from $140 \mu\text{mol L}^{-1}$ in the western tropics, over a time-scale of 100 years based on the western vs. eastern difference in ^{14}C at its minimum. Later, Johnson et al. (2006) used a similar approach for a regional NEPB estimate, relative to a $160 \mu\text{mol L}^{-1}$ value near Hawaii. Their updated inventory calculation resulted in an excess silica pool of approximately 164 Tmol between 2000-3000 dbar. A transit time set by a westward flow of 0.5 cm/s led to a flux of 2.4 Tmol/yr . If the transit time was instead set by the radiocarbon residence time (Talley and Joyce 1992), this value was reduced to 1.6 Tmol/yr .

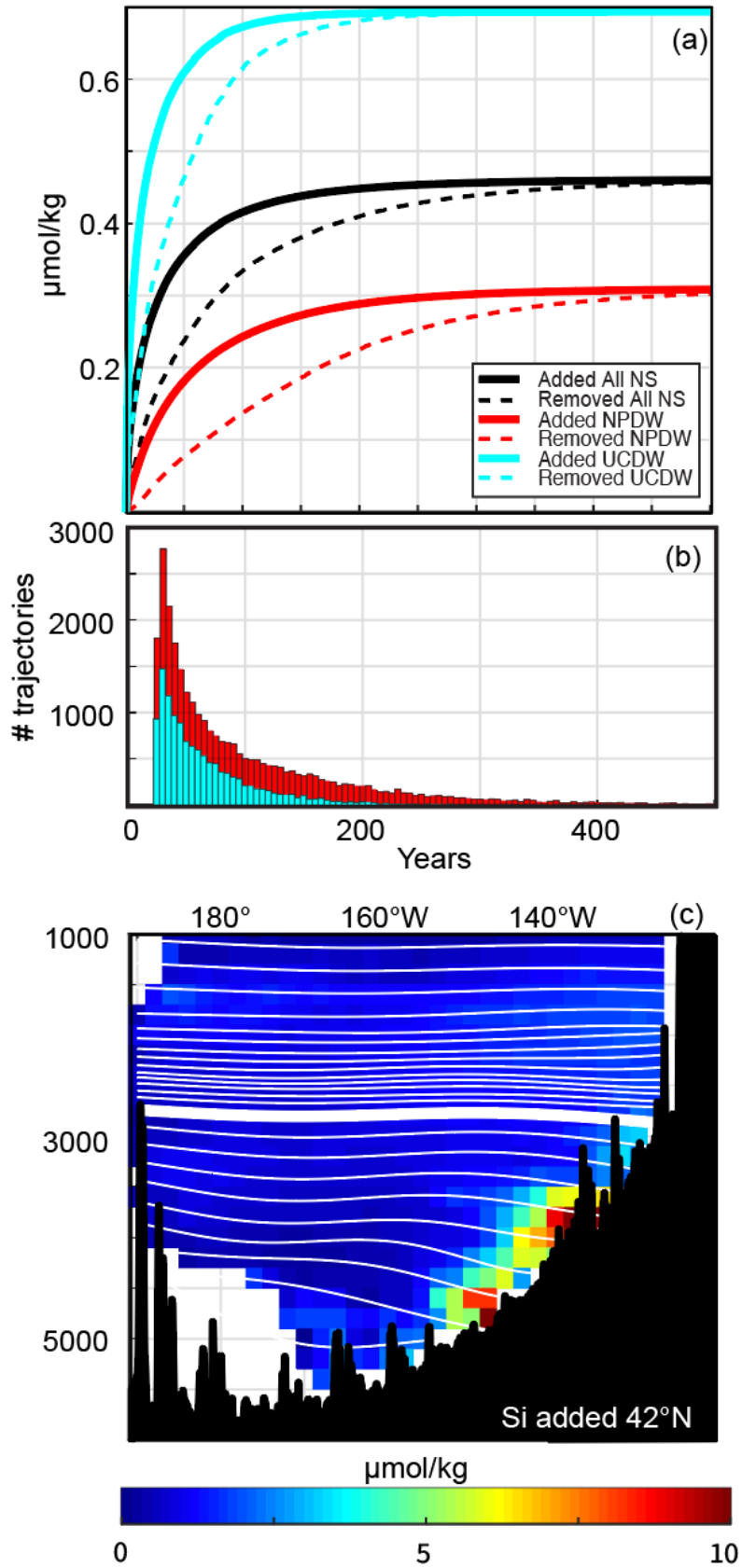


Figure 3. (a) Along-trajectory silica concentration as a function of years since initialization averaged over all water parcels (black), NPDW (red) and UCDW (blue). Solid lines show the average for all water parcels remaining within the basin. Dashed lines show the average for water parcels exiting at that time. (b) Distribution of time between release and exit for NPDW (blue) and UCDW (red). A large number of trajectories exit within 25 years across nearby boundaries and are excluded from this histogram. (c) Silica added (Eulerian bin-averaged) along 42°N, defined as concentration of a water parcel minus its initial value. White lines indicate neutral surfaces, with the uppermost UCDW model surface thickened.

Our preferred model run can be compared to these earlier estimates by using the combined mass of silica added to the Eulerian bins. For the NPDW as a whole (approximated as between 1000-2800 dbar), 29 Tmol is added. The source is primarily from water-column regeneration that is relatively uniform with depth and longitude (Figures 3c, S-B2, Table S-D1 comparing Si added in Runs 18 and 7). The average time since initialization, or age, is 86 years, and the average supply rate is 0.3 Tmol/yr, calculated by averaging individual values of added silica divided by age. The amount of silica added is sensitive to assumed parameter values (Table S-D1). The rate of silica addition, however, is not sensitive to changes in lateral diffusivity, although it is impacted by variations in the source strength (Table S-D1). In this mid-depth zone, the average supply rate is 5 to 10 times smaller than the earlier estimates, supporting the idea that the NPDW maximum is largely advecting through the model domain with relatively minor modification. The inverse model suggests that 0.1 cm/s is a more appropriate scale value for NPDW advective velocity (H18), explaining much of the difference from Johnson et al. (2006). In addition, the lower NPDW primarily enters the basin from the north, where it has been augmented by mid-depth Bering Sea outflow, raising the concentration of “background” silica water by 6 to 17 $\mu\text{mol/kg}$ (based on the zonal range of northern-line initial Si).

The model underpredicts Si below 2000 dbar (Figure 2c), a bias that cannot be corrected by tuning K_H without exacerbating low radiocarbon bias (Supplement, Section D). Along P17 (Figure 2b), the NPDW silica deficit is especially large south of $\sim 48^\circ\text{N}$, proximal to gaps in the Juan de Fuca Ridge where higher silica Cascadia Basin Bottom Water overflows (Hautala et al. 2009). Talley and Joyce (1992) hypothesized that Cascadia Basin was a source for mid-depth Si, however benthic flux measurements show that it can contribute only ~ 0.06 Tmol/y (Esther et al. 2010), about 20% of the overall NPDW input in our model. Although not properly resolved on the large scale of the inverse circulation fields, a sensitivity experiment with a crude representation of silica flux from Cascadia Basin suggests that its omission may be partially responsible for the regional low values in the tracer model at mid-depth along P17 (Figure S-D2).

In contrast to the situation at mid-depth, near-bottom UCDW model silica concentration is strongly modified within the NEPB. North of 30°N , UCDW primarily enters from the northern boundary, flowing southward along topography east of 150°W . This bottom-intensified southward flow is associated geostrophically with neutral surfaces that slope downward to the east (H18, Figures 1a, d and S-D3). Water parcels preferentially acquire silica from the bottom source in regions where these neutral surfaces ground, or incrop, into the seafloor that slopes upward to the east (Figure 3c). The incrop longitude shifts further east for lighter surfaces, resulting in lower silica water above higher silica water in the UCDW layer at any given location (Figure 1c, d). Consistently, a weak near-bottom maximum in total carbon is also created, in

agreement with the data along P01-2007 (for carbon fields, see the Supplement). At 4000 dbar, Si is elevated by 5-10 $\mu\text{mol/kg}$ over the initial value in an area east of 150°W (Figure 1c), before becoming admixed with lower Si water to the south. In total, the UCDW (2800-5000 m) gains 35 Tmol, primarily from the seafloor source. The average age is 40 years, and the average supply rate is 1.4 Tmol/year, primarily from the eastern subarctic gyre. A spatial correlation between young age and high silica flux makes the average supply rate substantially larger than the total silica added divided by the average age. This correlation also makes the supply rate in the UCDW more sensitive to variations in lateral diffusivity (Table S-D1) since K_H affects the time spent in proximity to localized seafloor sources.

We conclude:

(1) The mid-depth silica maximum (lower NPDW) is largely flowing through the basin with minimal modification of concentration, primarily from water column dissolution, consistent with the original hypothesis of Edmond et al. (1979). The increase in silica at the maximum towards the east along the Aleutian Trench creates an appearance of a focused source in the NEPB, but the vertical structure is largely established in the northwest Pacific via enhancement of an inherent mid-depth maximum that results from the greater “age” of the NPDW relative to the underlying UCDW, coupled with Bering Sea input.

(2) The near-bottom maximum in the UCDW is created locally within the basin, consistent with the independent analysis of Hou et al. (2019) based on benthic flux measurements and one-dimensional modeling of the bottom 500 m of the water column. The addition of silica via the seafloor source occurs preferentially where neutral surfaces incrop into broadly upsloping topography, a structure associated with the southward geostrophic flow pathway east of 150°W.

The observed silica structure is fundamentally dependent on little diapycnal transport between the UCDW and NPDW, supported by weak diapycnal mixing in H18. In the inverse model, the total Eulerian diapycnal transport across the $\sigma_{\theta}=28.01$ surface is only 0.1 Sv, about 3% of the 3.5 Sv abyssal inflow from the northern boundary below 3000 m. From the Lagrangian perspective, this volume transport is carried by only 0.6% of the seeded water mass trajectories, and all of these are initialized at the uppermost UCDW density, indicating a very “flat” aspect ratio to the overturning circulation, and allowing the double silica maximum to persist over a substantial portion of the NEPB.

The level of diapycnal mixing is considerably weaker than DeVries and Holzer (2019), and full verification awaits direct measurement. However, weak NEPB mixing is supported by the observations that do exist (Kunze 2017). Unresolved mixing hotspots, linked to topographic roughness, may provide localized places where water parcels move from the UCDW into the NPDW (H18). Indeed, high silica concentrations connect the deep and mid-depth maxima in a limited band just north of 40°N along P17 (Figure 2b). The Mendocino Fracture Zone may thus be one mixing hotspot – its crest reaches well into the NPDW, and diapycnal mixing rates are elevated in its immediate vicinity (Althaus et al. 2003).

Finally, given diapycnal mixing rates that decrease away from the seafloor, there is little diapycnal communication within the NPDW itself; its treatment as a single water mass is likely an oversimplification. Water parcels may exit the basin and recirculate west of the Hawaiian Ridge to re-enter the system at lighter density. Circuits including the southern hemisphere cannot be ruled out. In fact, although coverage is limited, greater similarity in mid-depth $\delta^{30}\text{Si}$ between

the NEPB and the eastern tropics, versus the interior subtropics west of Hawaii, may be evidence of such interhemispheric pathways (Beucher et al. 2008). The noncoincidence of diverse tracer extrema such as silica, oxygen, nutrients, carbon, radiocarbon and ^3He (e.g Fig. S-B1, S-B2, Lupton 1998; Talley et al. 1991) in the northeast Pacific has posed a puzzle. We hypothesize a new schematic involving a slow upward spiral of deep water parcels making multiple long circuits that pass through the Northeast Pacific Basin on successively lighter density horizons. This many-layered circulation system, combined with the unique source/sink aspects of each tracer feeding into different portions of the upward spiralling trajectories, may have better success in explaining the observed complexity in deep Pacific tracer features and improve understanding of processes that control the properties of deep water that ultimately returns to the Southern Ocean to impact the global thermohaline circulation.

Acknowledgments and Data

Data are in the public domain or otherwise published as noted in the text. The geostrophic flow fields and electronic Supplement are permanently archived at UW ResearchWorks (<http://hdl.handle.net/1773/45615> and <http://hdl.handle.net/1773/45615>). We appreciate the thoughtful comments of two anonymous reviewers.

References

- Althaus, A. M., E. Kunze and T. B. Sanford (2003). Internal tide radiation from Mendocino Escarpment. *J. Phys. Ocean.* 33: 1510-1527.
- Beucher, C. P., M. A. Brzezinski and J. J. Jones (2008). Sources and biological fractionation of Silicon isotopes in the Eastern Equatorial Pacific. *Geochim. Et Cosmochim. Acta* 72: 3063-3073.
- DeVries, T. and M. Holzer (2019). Radiocarbon and helium isotope constraints on deep ocean ventilation and mantle- ^3He sources. *J. Geophys. Res.:* 2018JC014716.
- Edmond, J. M., S. S. Jacobs, A. L. Gordon, A. W. Mantyla and R. F. Weiss (1979). Water column anomalies in dissolved silica over opaline pelagic sediments and the origin of the deep silica maximum. *J. Geophys. Res.* 84 (C12): 7809-7926.
- Esther, T. A., D. E. Hammond, S. L. Hautala, H. P. Johnson, R. J. Schwartz and A. N. Paukert (2010). Evaluation of the budget for silicic acid in Cascadia Basin deep water. *Deep-Sea Research I* 57: 677-686.
- Feely, Richard A.; Sabine, Christopher L.; Millero, Frank J.; Langdon, Chris; Fine, Rana A.; Bullister, John L.; Hansell, Dennis A.; Carlson, Craig A.; McNichol, Ann; Key, Robert M.; Byrne, Robert H.; Wanninkhof, Rik (2013). Partial pressure (or fugacity) of carbon dioxide, dissolved inorganic carbon, pH, alkalinity, temperature, salinity and other variables collected from discrete sample and profile observations using Alkalinity titrator, CTD and other instruments from THOMAS G. THOMPSON in the Gulf of Alaska, North Pacific Ocean and South Pacific Ocean from 2006-02-13 to 2006-03-30 (NODC Accession 0108062). Version 2.2. National Oceanographic Data Center, NOAA.
- Hammond, D. E., J. McManus and W. M. Berelson (2004). Oceanic germanium/silicon ratios: Evaluation of the potential overprint of temperature on weathering signals. *Paleoceanography* 19: doi:10.1029/2003P A000940

- Hautala, S. L., H. P. Johnson and D. E. Hammond (2009). Bottom water circulation in Cascadia Basin. *Deep-Sea Res. I* 56, 1688–1707.
- Hautala, S. L. (2018). The abyssal and deep circulation of the Northeast Pacific Basin. *Prog. Oceanogr.* 160: 68-82.
- Hou, Y., D. E. Hammond, W. M. Berelson, N. Kemnitz, J. F. Adkins and A. Lunstrum (2019). Spatial patterns of benthic silica flux in the North Pacific reflect upper ocean production. *Deep-Sea Res. I* 148: 25-33.
- Johnson, H. P., S. L. Hautala, T. A. Bjorklund and M. R. Zarnetske (2006). Quantifying the North Pacific silica plume. *Geochemistry, Geophysics and Geosystems* 7: doi:10.1029/2005GC001065.
- Kawano, T., H. Uchida and T. Doi (2009). WHP P01, P14 Revisit Data Book: Field Activity of JAMSTEC towards International Repeat Hydrography and Carbon Program, 2007. Japan Agency for Marine-Earth Science and Technology.
- Key, R.M., A. Olsen, S. van Heuven, S. K. Lauvset, A. Velo, X. Lin, C. Schirnick, A. Kozyr, T. Tanhua, M. Hoppema, S. Jutterström, R. Steinfeldt, E. Jeansson, M. Ishii, F. F. Pérez, and T. Suzuki (2015). Global Ocean Data Analysis Project, Version 2 (GLODAPv2), ORNL/CDIAC-162, ND-P093. Carbon Dioxide Information Analysis Center, Oak Ridge National Laboratory, US Department of Energy, Oak Ridge, Tennessee. doi:10.3334/CDIAC/OTG.NDP093_GLODAPv2
- Kunze, E., Firing, E., Hummon, J.M., Chereskin, T.K., Thurnherr, A.M., (2006). Global abyssal mixing inferred from lowered ADCP shear and CTD strain profiles. *J. Phys. Oceanogr.* 36, 1553–1576.
- Kunze, E. (2017). Internal-wave-driven mixing: global geography and budgets. *J. Phys. Ocean.* 47: 1325-1345.
- Macdonald, A.M., Mecking, S., Robbins, P.E., Toole, J.M., Johnson, G.C., Talley, L., Cook, M., Wijffels, S.E., 2009. The WOCE-era 3-D Pacific Ocean circulation and heat budget. *Prog. Oceanogr.* 82, 281–325.
- Marsay, C.M., R.J. Sanders, S.A. Henson, K. Pabortsava, E.P. Achterberg, and R.S. Lampitt (2015) Attenuation of sinking particulate organic carbon flux through the mesopelagic ocean. *Proc. Nat. Acad. Sci.* 112 (4): 1089-1094.
- Martin, J. H., G. Knauer, D. Karl, D. and W. Broenkow (1987). VERTEX: Carbon cycling in the northeast Pacific, *Deep-Sea Res. I* 34: 267–285.
- Musgrave, D., M. Aoyama, R. M. Key and P. D. Quay (1995). Final Cruise Report: World Ocean Circulation Experiment Pacific Ocean P17N. CLIVAR and Carbon Hydrographic Data Office. https://cchdo.ucsd.edu/cruise/325021_1.
- Olsen, A., R. M. Key, S. van Heuven, S. K. Lauvset, A. Velo, X. Lin, C. Schirnick, A. Kozyr, T. Tanhua, M. Hoppema, S. Jutterström, R. Steinfeldt, E. Jeansson, M. Ishii, F. F. Pérez and T. Suzuki (2016). The Global Ocean Data Analysis Project version 2 (GLODAPv2) – an

- internally consistent data product for the world ocean, *Earth Syst. Sci. Data*, 8, 297–323, doi:10.5194/essd-8-297-2016.
- Owens W. B. and B. A. Warren (2001). Deep circulation in the northwest corner of the Pacific Ocean. *Deep-Sea Res. I*: 48 :959-993, doi:10.1016/S0967-0637(00)00076-5.
- Reed R. K., G. V. Khen, P. J. Stabeno, A. V. Verkhunov (1993). Water properties and flow over the deep Bering Sea basin, summer 1991. *Deep-Sea Res. I*. 40:2325-2334.
- Rye et al. (2012). Diapycnal diffusivities from a tracer release experiment in the deep sea, integrated over 13 years. *Geophys. Res. Lett.* 39: 2011GL050294.
- Schmitz Jr, W.J., 1995. On the interbasin-scale thermohaline circulation. *Rev. Geophys.* 33, 151–173.
- Swift, James H.; Mecking, Sabine; Feely, Richard A.; Dickson, Andrew G.; Carlson, Craig A.; Jenkins, William J.; McNichol, Ann; Key, Robert M.; Ho, David T.; Sigman, Daniel; Macdonald, Alison M.; Buesseler, Ken; Martz, Todd R. (2014). Dissolved inorganic carbon, pH, alkalinity, temperature, salinity and other variables collected from discrete sample and profile observations using CTD, bottle and other instruments from MELVILLE in the North Pacific Ocean and Philippine Sea from 2013-03-21 to 2013-05-01 (NODC Accession 0117338). Version 3.3. National Oceanographic Data Center, NOAA. Dataset. doi:10.3334/CDIAC/OTG.GOSHIP_P02_318M20130321
- Talley, L. D., T. M. Joyce and R. A. de Szoeki (1991). Transpacific sections at 47°N and 152°W: distribution of properties. *Deep-Sea Res.*, 38 (S1): S63-S82.
- Talley, L. D. and T. M. Joyce (1992). The double silica maximum in the North Pacific. *J. Geophys. Res.* 97 (C4): 5465-5480.
- Taylor, G. I. (1921). Diffusion by continuous movements. *Proc. London Math. Soc.*, 20, 196-212.
- Van Sebille, E., et al. (2018). Lagrangian ocean analysis: Fundamentals and practices. *Oc. Model.* 121: 49-75.
- Tsunogai, S. (1987). Deep-water circulation in the North Pacific deduced from Si-O diagrams. *J. Oceanogr. Soc. Japan*, 43: 77-87.
- Warren, B. A. and W. B. Owens (1985). Some preliminary results concerning deep northern-boundary currents in the North Pacific. *Prog. Oceanogr.* 14, 537–551.
- Wong, C.S., F.A. Whitney, D.W. Crawford, K. Iseki, R.J. Matear, W.K. Johnson, J.S. Page, and D. Timothy (1999). Seasonal and interannual variability in particle fluxes of carbon, nitrogen and silicon from time series of sediment traps at Ocean Station P, 1982-1993: relationship to changes in subarctic primary productivity, *Deep-Sea Res. II* 46, 2735-2760, 1999.



Geophysical Research Letters

Supporting Information for

Abyssal Pathways and the Double Silica Maximum in the Northeast Pacific Basin

Susan L. Hautala¹ and Douglas E. Hammond²

¹University of Washington.

²University of Southern California.

Contents of this file

- A. Lagrangian trajectory tracer initialization values (Figure S-A1).
- B. Additional model fields (Figures S-B1, S-B2).
- C. Additional model-data comparisons (Figure S-C1).
- D. Sensitivity experiment (Table S-D1, Figures S-D1 through S-D5).

Introduction

This supplement contains information about the boundary conditions (supplemental to Figure 1), along with additional model fields and comparisons to observations (supplemental to Figures 1-3).

The final section (D) contains a detailed discussion of the sensitivity experiments that were summarized in the text, with additional supporting figures.

A. LAGRANGIAN TRAJECTORY TRACER INITIALIZATION VALUES

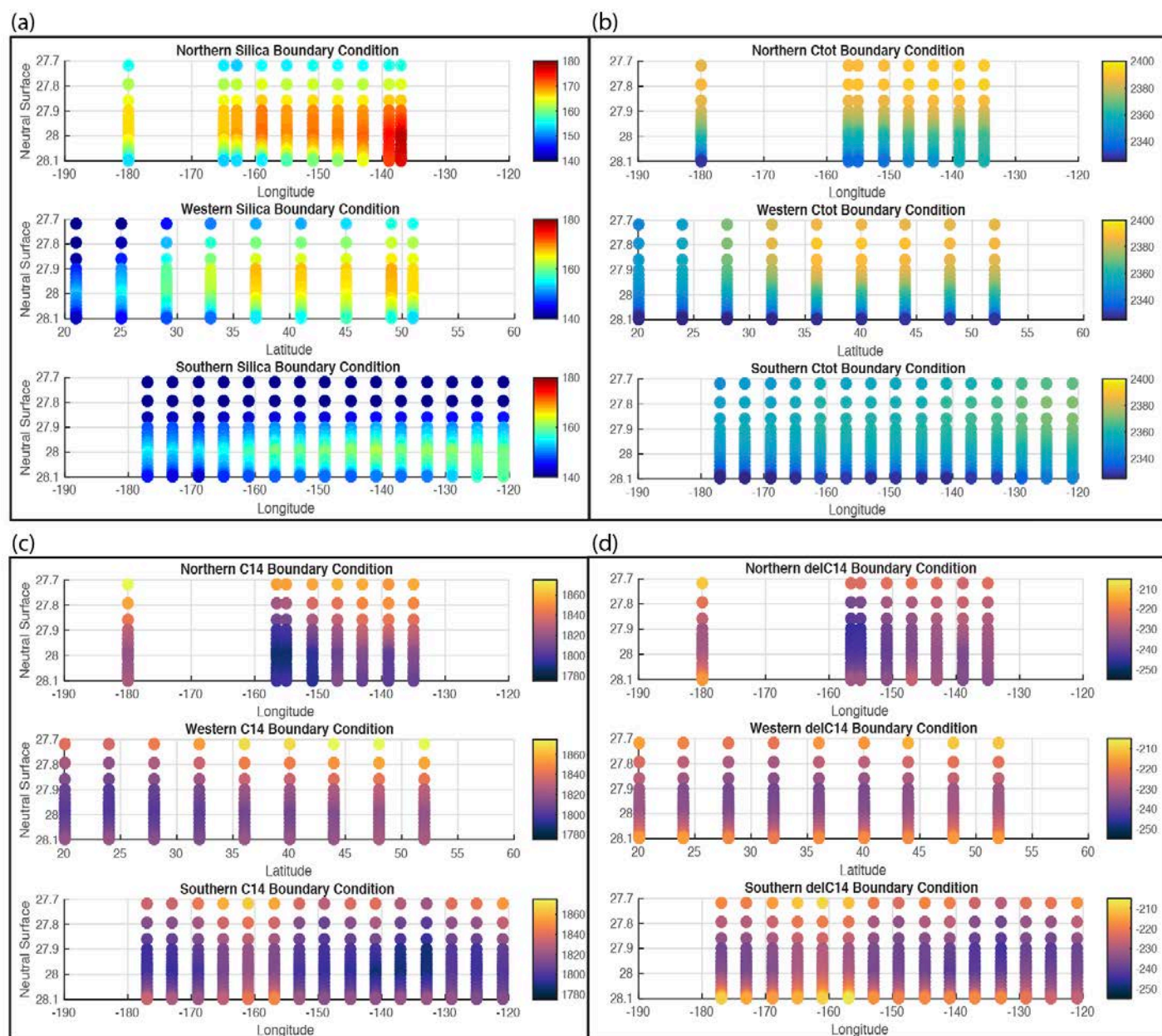


Figure S-A1. Tracer concentration boundary conditions for water parcel trajectories initialized along northern, western, and southern lines: (a) Silica ($\mu\text{mol kg}^{-1}$), (b) total Carbon ($\mu\text{mol kg}^{-1}$), (c) ^{14}C normalized by $^{14}\text{C}/^{12}\text{C}$ ratio in 1950 atmosphere ($\mu\text{mol kg}^{-1}$), (d) $\Delta^{14}\text{C}$ (‰), calculated from (b) and (c).

B. ADDITIONAL MODEL FIELDS

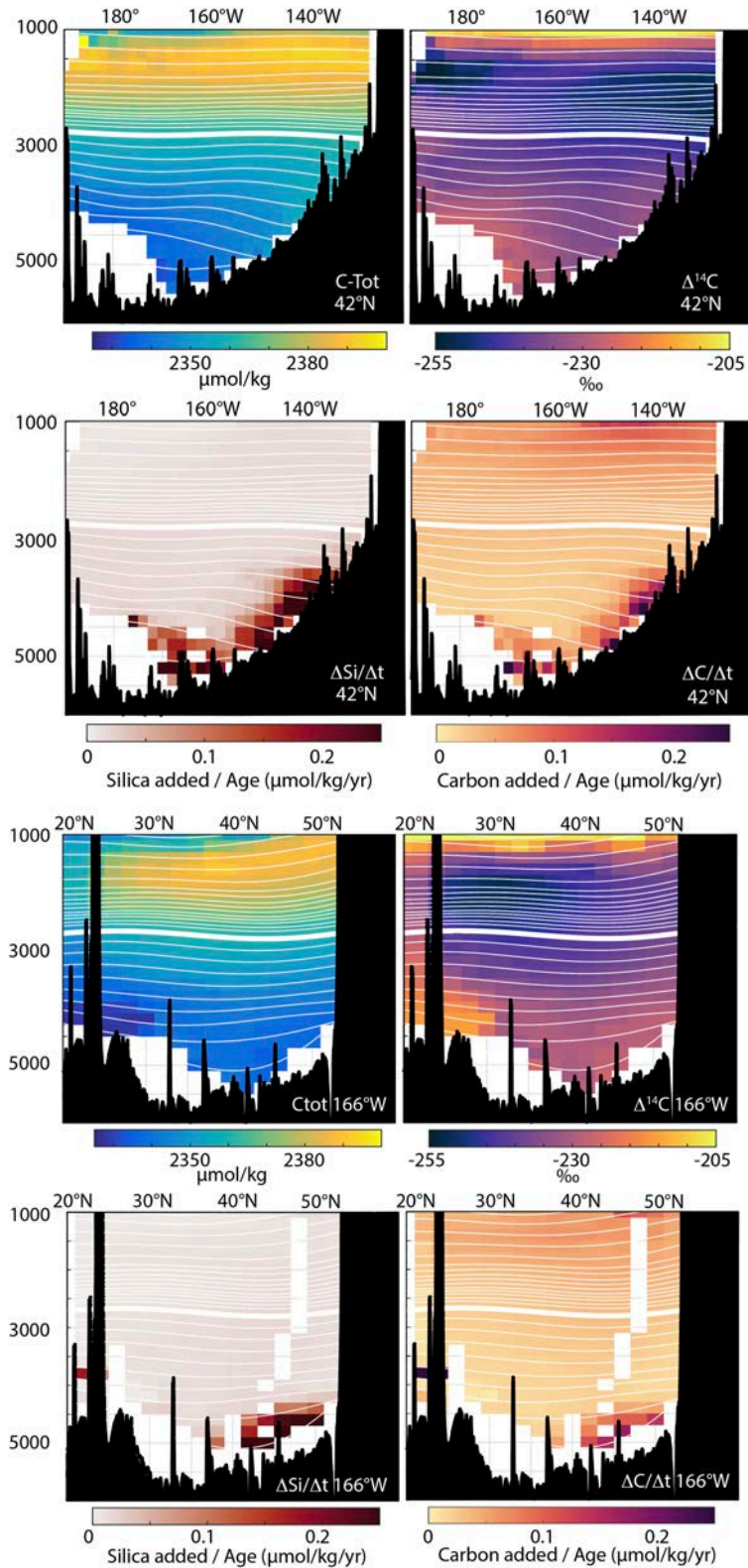


Figure S-B1. Additional bin-averaged tracer fields, as labelled. Tracer added is the value for a Lagrangian water parcel found at a given location minus its initial value. Thus, the rates in the lower panels average the time history of Lagrangian parcels found at a given location, and should not be interpreted as a local (Eulerian) flux rate.

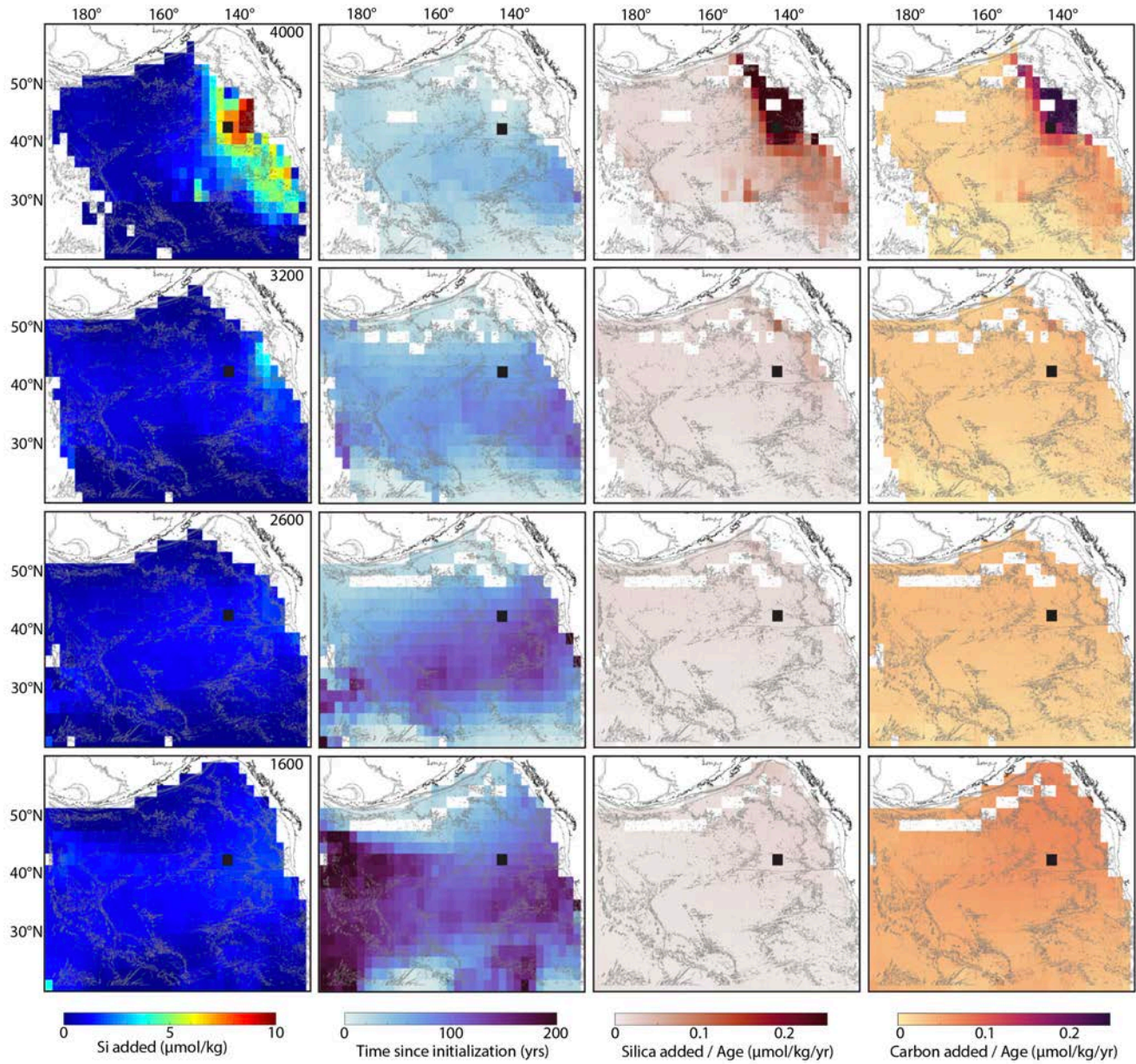


Figure S-B2. Additional bin-averaged variables, on pressure (dbar) surfaces as labelled. The black square marks 42°N, 142°W. Tracer added is the value for a Lagrangian water parcel found at a given location minus its initial value. Thus, the rates in the last two columns average the time history of Lagrangian parcels found at a given location, and should not be interpreted as a local (Eulerian) flux rate.

C. ADDITIONAL MODEL DATA COMPARISONS

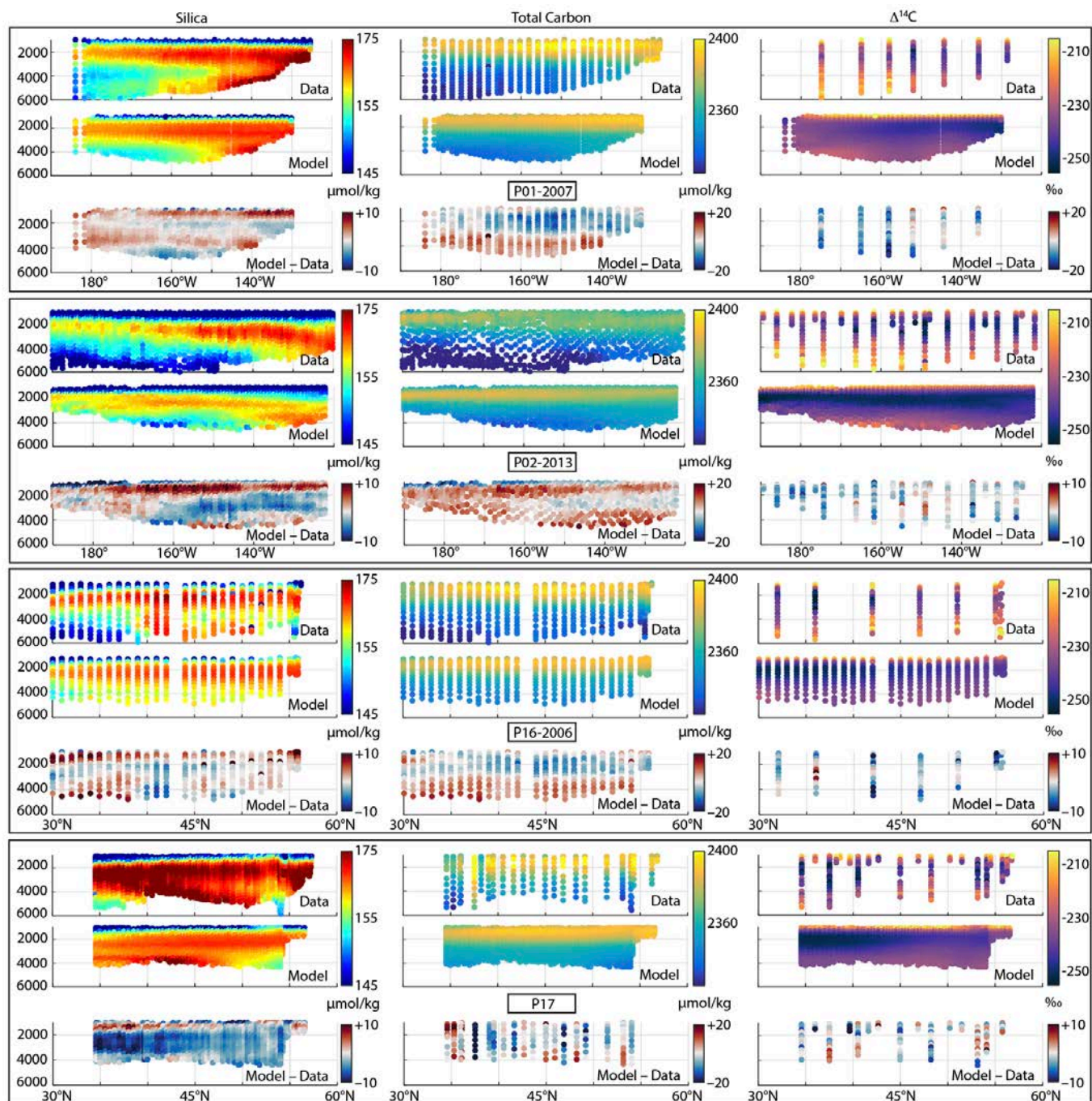


Figure S-C1. Modeled tracer fields interpolated to bottle data locations from hydrographic sections and the model concentration difference from the data. Note that because it is constrained to the UCDW, the model fields do not extend into topographically disconnected pools of denser LCDW in the north and south NEPB. Top row: P01-2007 along nominal 47°N; 2nd row: P02-2013 along ~30°N; 3rd row: P16-2006 along ~150°W; bottom row: P17 along ~135°W but angling to 160°W in the subarctic gyre.

D. SENSITIVITY EXPERIMENTS

Systematic variations to the assumed parameters were explored using 25 realization runs as listed in Table S-D1. It was found that the average radiocarbon bias, relative to the four sections of bottle data, was the most sensitive to variations of the lateral diffusivity, K_H , because of this tracer’s inherent decay-related clock. In each case, a new inverse model solution (following Hautala 2018) was computed (Figure S-D3), where the value of lateral diffusivity was specified rather than solved for. As K_H is varied, the magnitude of the radiocarbon bias is affected in opposite sense to the magnitude of the silica bias, and also to RMS misfits to the potential vorticity and salinity constraints in the inverse calculation (Figure S-D1), providing a means of selecting this parameter. A final choice was made by considering the improved radiocarbon agreement with increasing K_H , traded off against the size of the estimated 95% confidence limit error bars for any neutral surface ($\pm 211 \text{ m}^2/\text{s}$) for the inverse solution of Hautala (2018), as well as the adverse impact of increasing K_H on silica bias and inverse model misfit. The existence of the double silica maximum is not dependent on this choice (Figure S-D5). A 100-realization version with the parameters of Run 7 ($K_H = 260 \text{ m}^2/\text{s}$) is interpreted in the main paper. For this solution, the radiocarbon bias is approximately 1% between 1500-3500 m depth, comparable to the error level in deVries et al. (2019). A run that halts trajectories when they dead-end at topographic holes, rather than implementing the “boundary slippage” algorithm (Figure S-D4, compare to Figure 1) loses a great deal of information, especially in the deeper UCDW. However, again the double silica maximum still occurs.

Run	σ km	$K_H = 1/2 \sigma^2/\Delta t$ m^2/s	Si_Benthic x [20, 200, 600] $\text{mmol}/\text{m}^2/\text{yr}$	Si_Rain x [1, 10, 90] $\text{mmol}/\text{m}^2/\text{yr}$	CB_Source H value (m)	Si Added (Tmol) / $\Delta\text{Si}/\Delta t$ (Tmol/y) 1000-2800	Si Added (Tmol) / $\Delta\text{Si}/\Delta t$ (Tmol/y) 2800-5000
1	40	51	[1,1,1]	[1,1,1]	0	55.8 / 0.33	58.3 / 1.96
2	50	81	[1,1,1]	[1,1,1]	0	51.9 / 0.34	62.8 / 2.00
3	60	116	[1,1,1]	[1,1,1]	0	45.9 / 0.35	53.5 / 1.83
4	70	158	[1,1,1]	[1,1,1]	0	39.0 / 0.34	42.4 / 1.55
5	80	206	[1,1,1]	[1,1,1]	0	33.3 / 0.34	41.0 / 1.54
6	85	232	[1,1,1]	[1,1,1]	0	30.9 / 0.34	38.0 / 1.57
7*	90	260	[1,1,1]	[1,1,1]	0	28.3 / 0.34	32.8 / 1.48
8	100	322	[1,1,1]	[1,1,1]	0	24.5 / 0.37	29.5 / 1.48
9	90	260, no KV	[1,1,1]	[1,1,1]	0	28.6 / 0.34	35.9 / 1.38
10	90	260	[1,1,1]	[1,1,1]	10	51.4 / 0.53	37.2 / 1.67
11	90	260	[1,1,1]	[1,1,1]	50	34.4 / 0.39	32.5 / 1.41
12	90	260	[1,1,1]	[1,1,1]	100	31.5 / 0.36	33.3 / 1.45
13	90	260	[1,1,2]	[1,1,0.5]	0	15.9 / 0.19	49.4 / 2.44
14	90	260	[1,2,1]	[1,0.5,1]	0	27.0 / 0.33	33.9 / 1.46
15	90	260	[1,2,2]	[1,0.5,0.5]	0	14.8 / 0.18	47.5 / 2.67
16	90	260	[1.05,1.05,1.15]	[0,0,0]	0	1.0 / 0.02	22.0 / 1.19
17	90	260	[1,1,1]	[1,1,0.33]	0	11.0 / 0.13	27.5 / 1.25
18	90	260	[0,0,0]	[1,1,1]	0	26.6 / 0.32	12.6 / 0.29

Table S-D1. Sensitivity study parameters using 25 realization averages. The total addition of silica in NPDW and UCDW layers during one pass of the water parcels through the basin is reported in the final two columns. Note that for Run 7, a 100 realization run is discussed in the text, leading to minor differences in the values mentioned there.

Random Gaussian displacement:

Runs 1-8 explored the effects of varying the value of the lateral (along neutral surface) displacement after each time step (equivalently, K_H). Larger values of lateral diffusivity increase the misfit in the potential vorticity and salinity conservation equations that are the basis of the circulation inverse model (Figure S-D1 top left). As a final experiment (Run 9), the diapycnal displacement (corresponding to K_V) is set to zero, with only minor impact on bias. The existence of the double silica maximum structure does not depend on the selected value of K_H although the concentration of the near-bottom maximum is reduced as K_H is increased.

Cascadia Basin source:

Runs 10-12 explored the addition of a Cascadia Basin source. If, after a given time-step, a trajectory point was located east of 132°W, between 44°N and 48°N and between 2100 to 2700 dbar, the silica flux was augmented by 0.81 mmol/m²/yr (Esther et al. 2010), divided by a (boundary layer) height indicated in the 6th column of Table S-D1, converted to μmol/kg/yr. Adding the most extreme version of the Cascadia Basin source (dividing the total flux by the smallest vertical layer thickness (10 m) modestly improved the basin wide average Si bias, particularly improving agreement along P17 for the mid-depth maximum (Figure S-D2).

Silica source function:

Runs 13-17 explored modifications of aspects of the silica source function. While the total amount of silica (right columns of Table S-D1) is impacted, there is little change in basin-average bias (Figure S-D1). Because silica tends to be biased low below 2000 m and biased high above that level, we explored increasing the bottom source in the transitional and subarctic bands separately and then together while halving the water column source. Next (Run 16), we set the water column source to zero and increased the bottom source proportionally. In Run 17, we set the subarctic water column source to 5% of the bottom source (the same percentage as the other latitude bands). Finally (Run 18), we set the bottom source to zero. Although the total amount of silica added to the basin is impacted by changes in source fluxes as expected (Table S-D1), there is no particular improvement in bias relative to Run 7 (Figure S-D1).

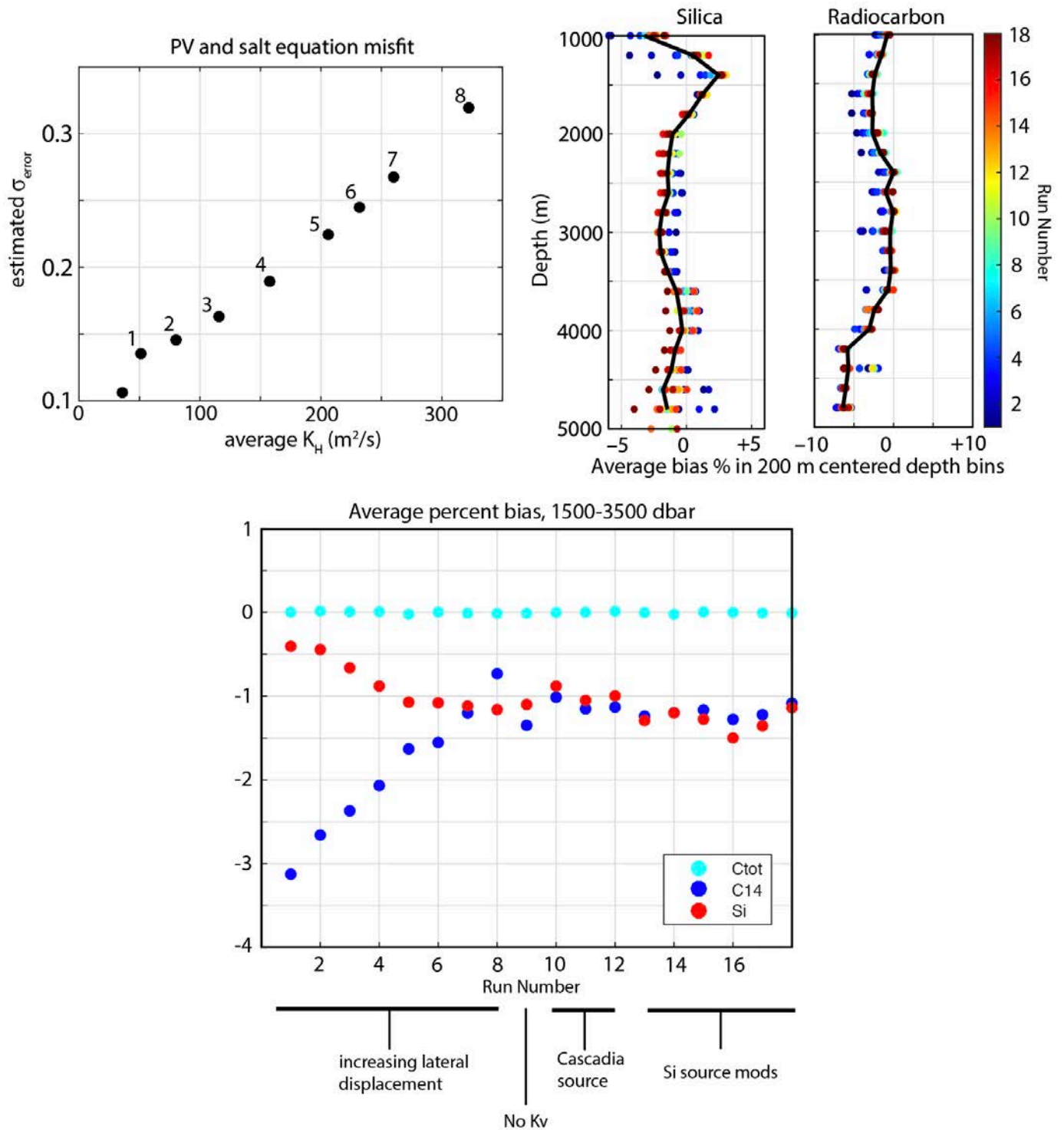


Figure S-D1. Top left: RMS error standard deviation from the inverse fit to potential vorticity and salinity equations using specified values of lateral diffusivity. The left-most data point corresponds to the solution in Hautala (2018) which has a depth-averaged $K_H = 36 \text{ m}^2/\text{s}$. Values for sensitivity run numbers (Table S-D1) are indicated next to the points. Top right: Average percent bias for silica and radiocarbon as a function of depth (compared to the four repeat hydrography sections discussed in the main text) colored by run number. Bottom: Average percent bias for 1500-3500 m as a function of run number for each of the three simulated tracers.

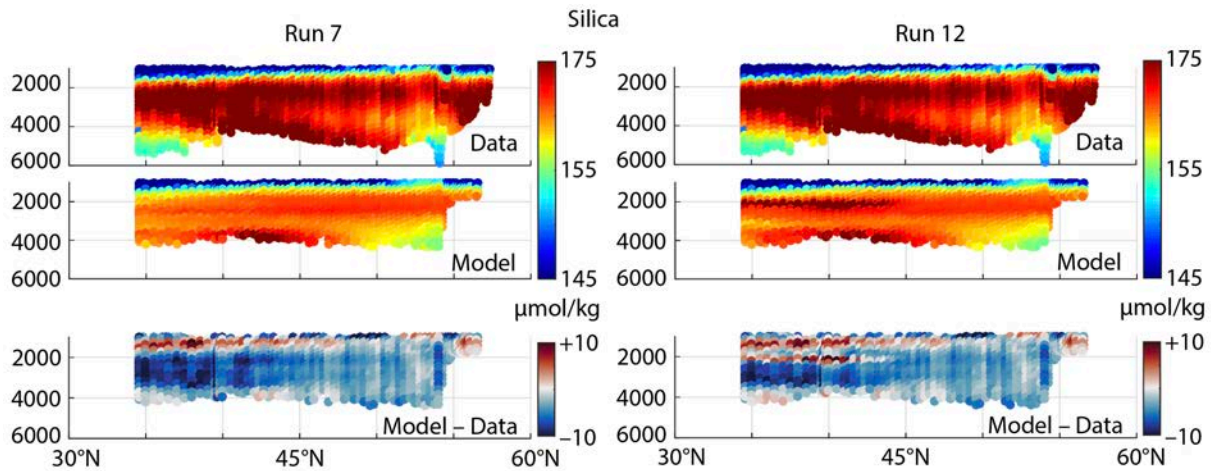


Figure S-D2. Model-data comparison along P17 without (Run 7) and with (Run 12) a crude Cascadia Basin silica source. Of the three experiments with this additional source, Run 12 distributes the estimated seafloor source from Esther et al. (2010) over the smallest depth range (10 m, see Table S-D1) and thus has the greatest impact on concentration.

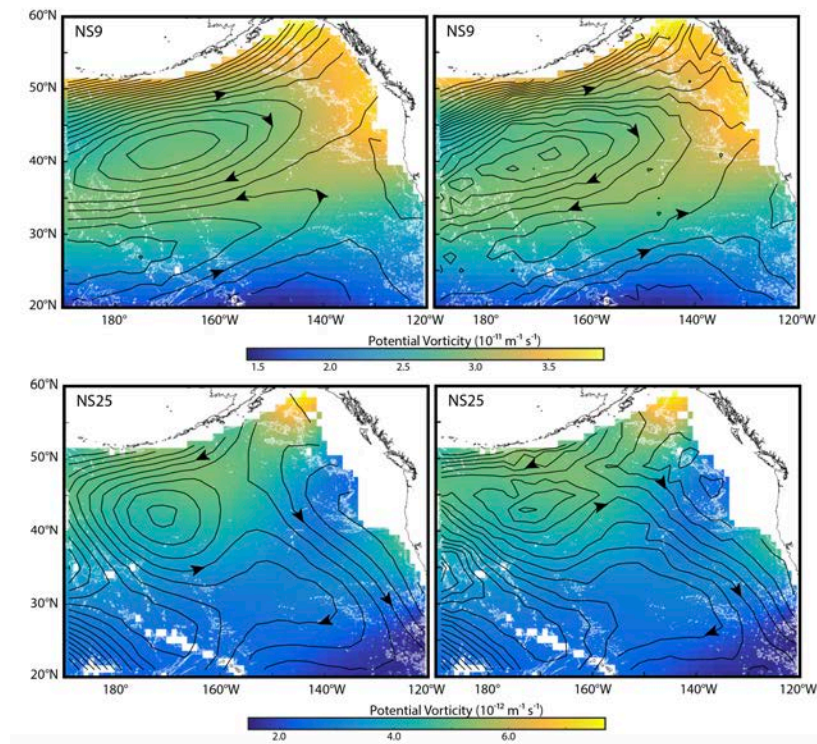


Figure S-D3. *Left*: Inverse model flow fields and potential vorticity where the lateral diffusivity is solved for as a least-squares fit to potential vorticity and salinity conservation equations (Hautala 2018). *Right*: Flow and potential vorticity from an inverse solution where lateral diffusivity is specified at $K_H = 260 \text{ m}^2/\text{s}$ (Run 7 value). Potential vorticity is colored and absolute geostrophic streamfunction is contoured in black (by $0.02 \text{ m}^2/\text{s}^2$) with flow directions indicated. *Top*: $\gamma = 27.795 \text{ kg m}^{-3}$, lying in the middle of the NPDW. *Bottom*: $\gamma = 28.072 \text{ kg m}^{-3}$, lying in the middle of the UCDW. Increased misfit in the potential vorticity and salinity equations with increasing lateral diffusivity manifests as noise in the right panel streamfunction contours.

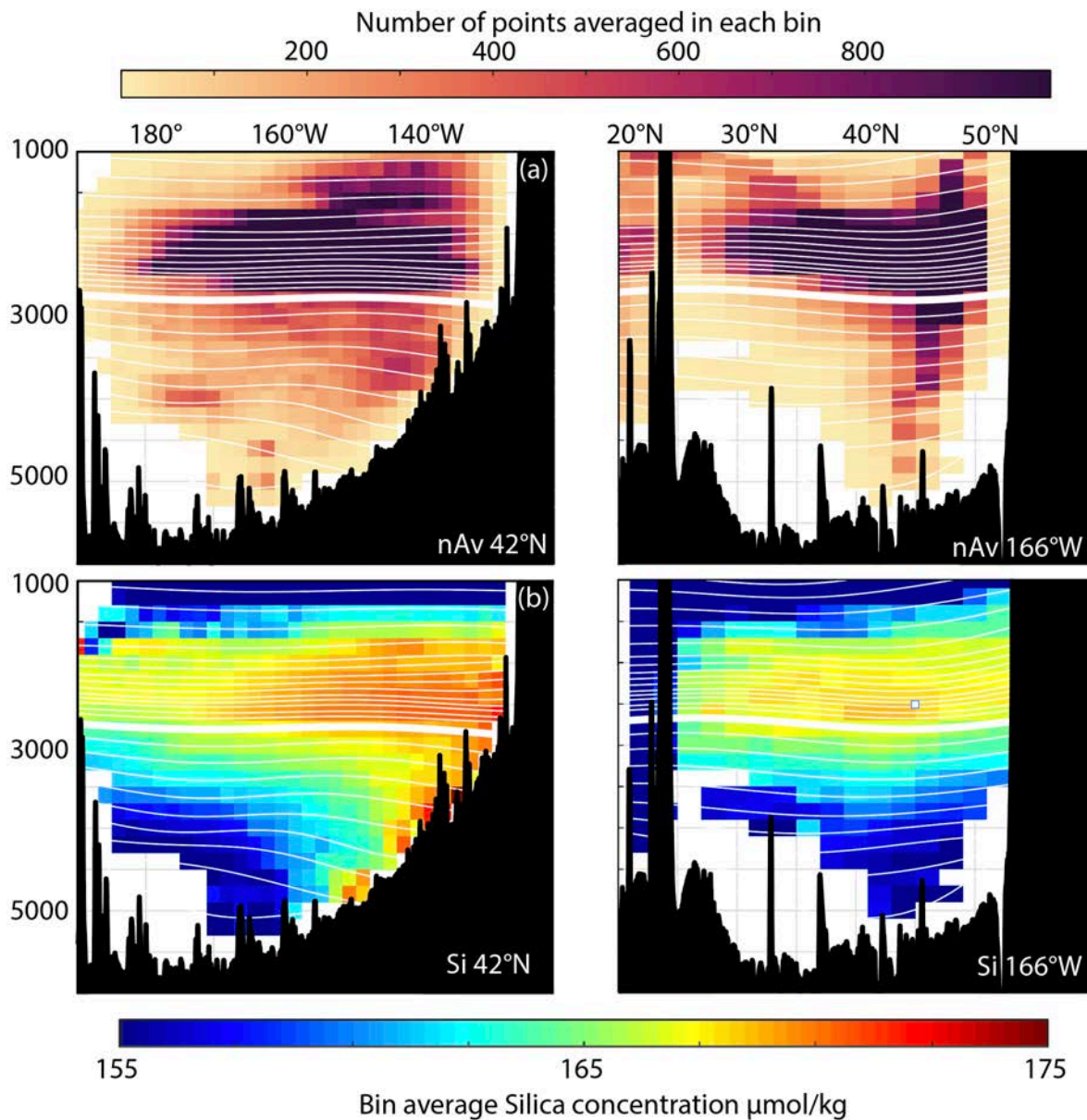


Figure S-D4. Vertical sections (see Figure 1 for comparison) for a 100 realization run where the boundary slippage algorithm is turned off. While the number of points to average for each Eulerian bin decreases, particularly in the UCDW, the double silica maximum still emerges.

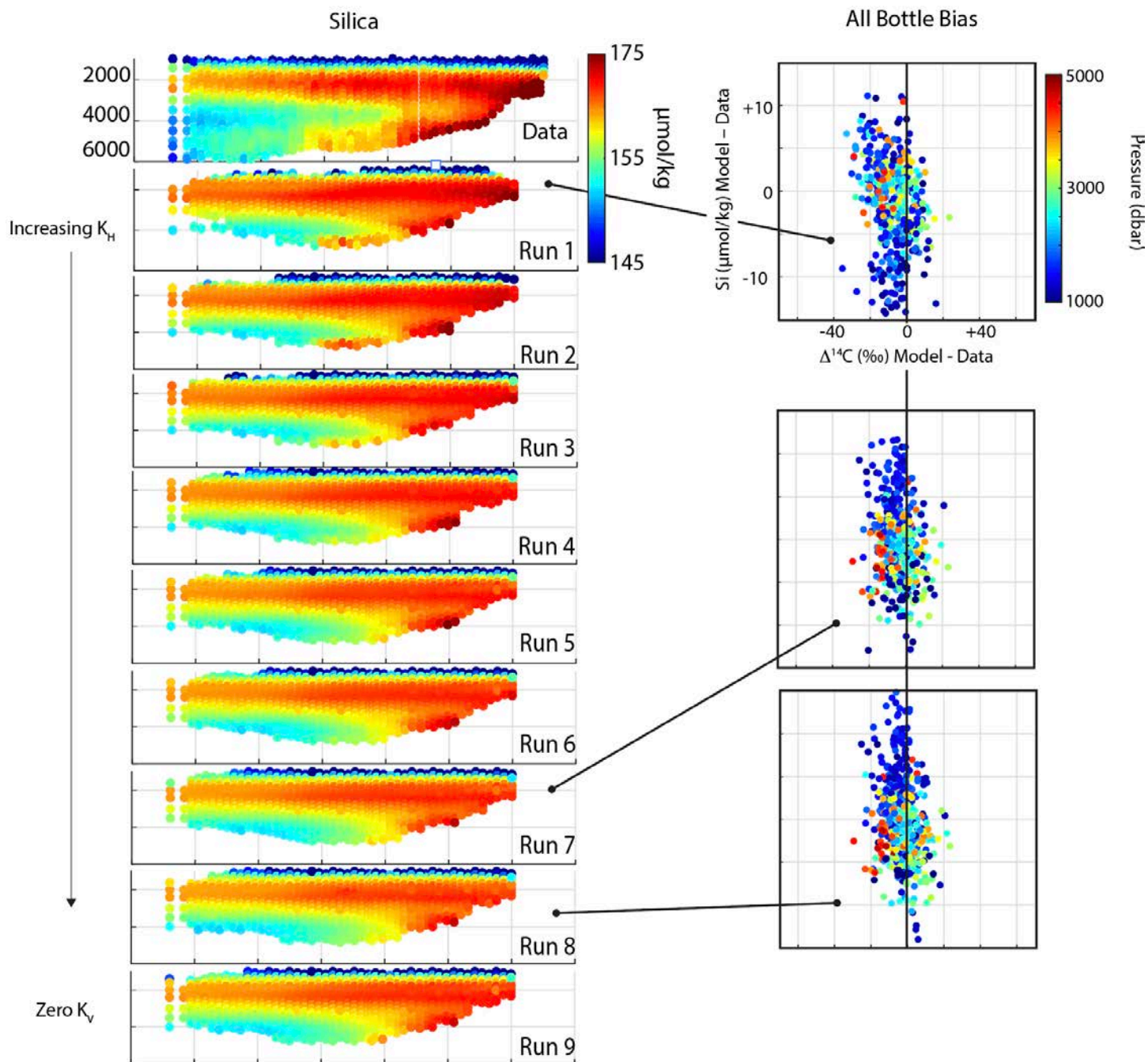


Figure S-D5. Bottle silica concentrations from data along P01-2007 (top, repeated on second page), and for model Runs 1 – 9, with notes indicated along left margin (see Table S-D1). At the right are radiocarbon vs. silica model bias scatter plots for selected runs. The series is continued on the next page.

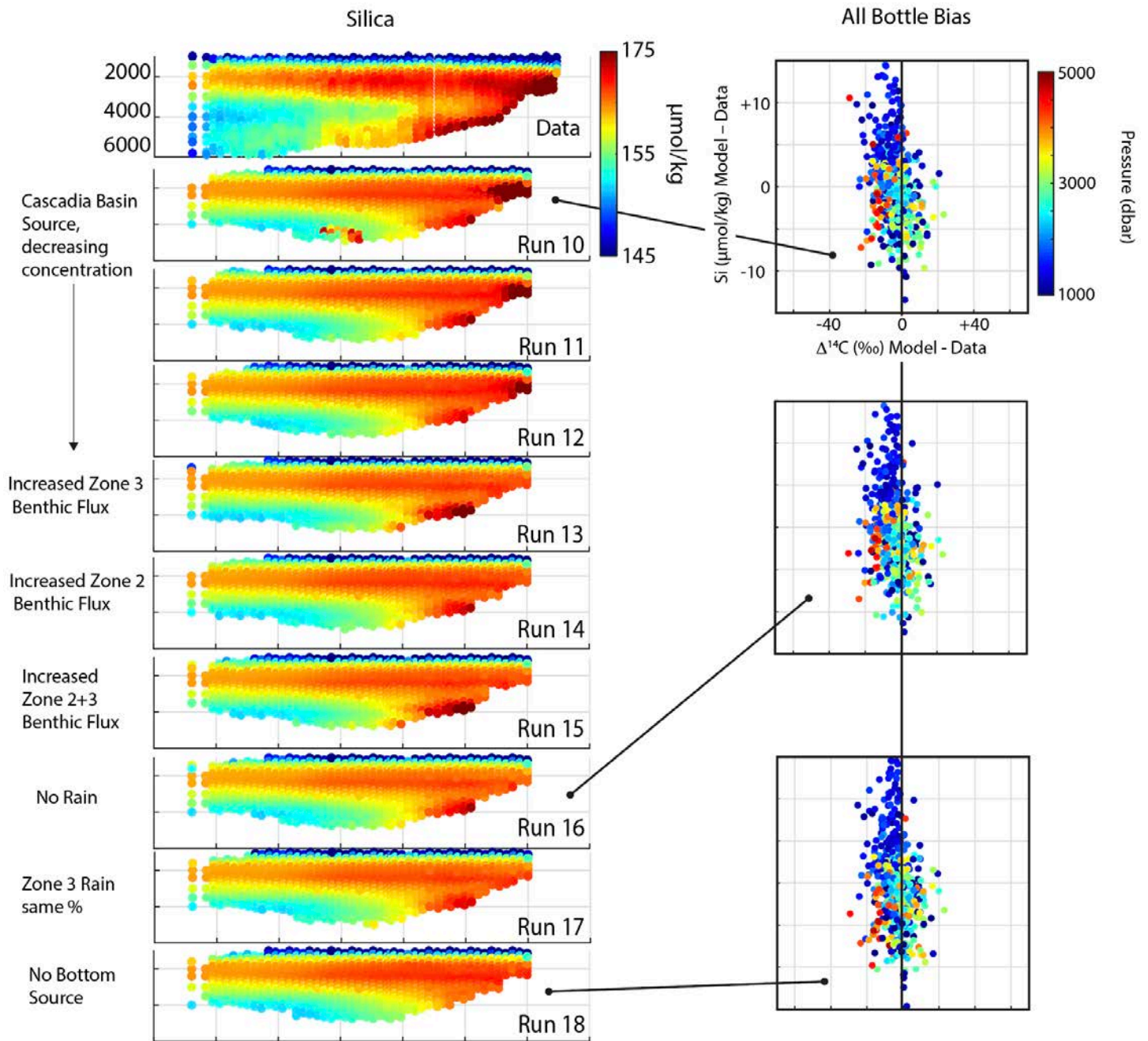


Figure S-D5 (continued). Bottle silica concentrations from data along P01-2007 (top), and for model Runs 10 – 18, with notes indicated along left margin (see Table S-D1). At the right are radiocarbon vs. silica model bias scatter plots for selected runs.